RSC Advances

ROYAL SOCIETY OF CHEMISTRY

www.rsc.org/advances

Optimizing PVD conditions for electrochemical anodization growth of well–adherent Ta_2O_5 nanotubes on Ti–6Al–4V alloy

Masoud Sarraf [a,b], Bushroa Abdul Razak [a,b,c,d,*], Ali Dabbagh [a,e], Bahman Nasiri-Tabrizi [f,*], Noor Hayaty Abu Kasim [e], Wan Jefrey Basirun [g]

[a] *Center of Advanced Manufacturing and Material Processing, Department of Engineering, University of Malaya, Kuala Lumpur 50603, Malaysia*

[b] *Department of Mechanical Engineering, Faculty of Engineering, University of Malaya, 50603 Kuala Lumpur, Malaysia*

[c] *Department of Mechanical Engineering, Faculty of Engineering, University of UCLA, Los Angeles, CA 90032, United States*

[d] *Department of Mechanical and Aerospace Engineering, University of California, CA 90095-1597, United States*

[e] *Department of Restorative Dentistry, Faculty of Dentistry, University of Malaya, Kuala Lumpur, Malaysia*

[f] *Advanced Materials Research Center, Materials Engineering Department, Najafabad Branch, Islamic Azad University, Najafabad, Isfahan, Iran*

[g] *Department of Chemistry, Faculty of Science, University of Malaya, 50603 Kuala Lumpur, Malaysia*

***Corresponding author:**
Dr. A.R. Bushroa
bushroa@um.edu.my
Tel: +60379675239
Fax: +60379675330

Postal Address:
Department of Mechanical Engineering,
Faculty of Engineering Building,
University of Malaya, 50603
Kuala Lumpur, MALAYSIA.

****Corresponding author:**
Bahman Nasiri-Tabrizi (RA)
bahman_nasiri@hotmail.com
Tel: +989132275822
Fax: +983142291016

Postal Address:
Materials Engineering Department,
Najafabad Branch,
Islamic Azad University, Najafabad,
Isfahan, IRAN.

Abstract

Well–adherent tantalum pentoxide nanotubes (Ta_2O_5 NTs) were successfully grown on Ti–6Al–4V alloy (Ti64) through optimization of physical vapor deposition magnetron sputtering (PVDMS) followed by a two-step anodization and subsequent thermal treatment from 450 to 1000 °C for 1 h with a heating/cooling rate of 1 °C min^{-1}, under atmospheric conditions. The effective sputter yield during the magnetron sputtering process was achieved with a DC power of 350 W, temperature of 250 °C and a deposition time of 6 h. The results showed that the anodization time played a key role in the growth of the Ta_2O_5 NTs and microstructural evolution. The nanotubes pore size and tube length varied from 18 to 30 nm and 73 nm to ~ 4 μm as anodizing time rose from 30 s to 20 min, respectively. For the 450 °C annealed sample with the strongest adhesion, the scratch length, failure point and adhesion strength were 1024 μm, 863 μm and 2301 mN, respectively. The 450 °C annealed coating showed the highest wettability (lowest contact angle value) among the specimens. This multi-step approach could be considered for the design of various nanostructured titanium implant surfaces.

Keywords: Ta_2O_5 nanotubes; PVD; Adhesion strength; Anodizing; Wettability; Ti–6Al–4V.

1. Introduction

Numerous attempts have been made over the past few decades to identify suitable metallic biomaterials for orthopaedic applications. Titanium and titanium alloys are widely used in biomedical applications, particularly as load-bearing metal implants due to their desirable features, such as relatively low modulus, good fatigue strength, formability, machinability, corrosion resistance and biocompatibility. However, Ti and its alloys cannot meet all of the clinical necessities owing to the lack of osseointegration required for implant longevity. One of the possible solutions to improve the bone–implant contact and the healing process is the use of

bioceramic coatings on metal implants [1–4]. Unluckily, low fracture toughness, delamination and cracking of ceramic coatings are great obstacles for their widespread application. Recently, a new class of biomaterials have been utilized to acquire biological fixation of bone to metal implants in total hip and knee prosthesis [5,6].

Tantalum and its oxides are gathering attention in bone repair applications for the past few years, due to their high biocompatibility and bioactivity [7], which facilitate biological bonding to the natural hard tissue via the formation of a bone-like apatite layer [8–10]. Moreover, self-passivation of Ta surface trough formation of a stable oxide layer results in an excellent corrosion-erosion resistance in biological environment without significant weight or roughness change, compared to the conventional metallic implants [11,12]. However, the relatively high modulus of elasticity and bulk density of Ta-based biomaterials, prohibit their application in load-bearing implants [7,9]. Typically, the mechanical mismatch between the implant and bone tissue results in bone desorption and implant loosening, which increases the risk of clinical failure [13]. Therefore, Ta and its oxides are mostly utilized as thin porous coatings on substrates such as titanium alloys [9, 14–16]. Tantalum pentoxide coatings with nanotubular structures (Ta_2O_5 NTs) have shown exceptional osseointegration behavior, resulting in higher fixation ratios compared to those of conventional implants [7,17,18]. In general, Ta_2O_5NT coatings are mostly grown from a thin layer of Ta via the anodization technique, where their physical and mechanical features are controlled by adjustment of the anodization and subsequent annealing conditions. Table 1 summarizes the anodization and annealing conditions which have been previously utilized in the synthesis of Ta_2O_5 NTs [5, 19–29]. However, the NTs developed so far are relatively longer, which increases the delamination tendency of the coating layer [9].

<Table 1>

To the best of our knowledge, apart from the absence of a comprehensive study on the electrochemical anodization of as-deposited Ta thin film coating on biomedical Ti-6Al-4V alloy (Ti64), there are no reports on the effect of subsequent annealing on the microstructural evolution. In the present work, the surface modification of biomedical Ti64 with a Ta layer was performed by means of PVD magnetron sputtering and subsequent electrochemical anodization of the as-deposited layer. An optimization study on the PVD magnetron sputtering conditions (DC power, temperature and time) was carried out using the Taguchi method to improve the adhesion strength. Subsequently, the Ta_2O_5 NTs were grown by a two-step anodization technique using a DC power source. To crystallize the nanotubes, thermal annealing process was also done after the anodization process. The phase evolution, microstructural features, surface wettability, microhardness and adhesion strength of the coatings were examined to provide a clear understanding of the behavior of the product in the current operating conditions. This study will open up an exciting new field in the science and technology of advanced coatings.

2. Materials and methods

2.1. Taguchi design of experiments

Selection of the processing parameters and identification of the orthogonal array (OA) are considered the most crucial step in the experimental design of the Taguchi approach [30]. In this study, three influential parameters which are the DC power, temperature and time, each comprised of three different levels were examined. Hence, a standard $L_9(3^3)$ orthogonal array was developed in order to allow the verification of the interactions between the various parameters. The control parameters and their corresponding levels selected in the experimental design of the Taguchi approach are given in Table 2.

<Table 2>

2.2. Substrate preparation

The substrates were fabricated from titanium alloy Grade 5 (Ti-6Al-4V, E Steel Sdn. Bhd, Klang, Malaysia) plates with dimensions of 15 mm × 15 mm × 2 mm. The specimens were prepared by polishing with 800–2400 grit silicon-carbide emery papers, followed by wet-polishing using a diamond slurry and sonication in acetone for 10 minutes at 40 °C. The substrates were then washed three times with distilled water, followed by drying at 100 °C for an hour. The EDS analysis of the substrate (Ti64) is shown in Fig. 1.

<Fig. 1>

2.3. Deposition of Ta coating

The Ta thin film was deposited on Ti64 substrates using PVD magnetron sputtering technique (SG control engineering Pte Ltd series, Singapore) equipped by a pure Ta target (99.995%) with 150 mm distance from the substrate. The Ti64 substrates were ultrasonically washed sequentially in acetone and ethanol, prior to the deposition of the Ta layer. It should be noted that the oxide layer on the target was removed by pre-sputtering in an argon atmosphere. The chamber was then vacuumed to less than 2×10^{-5} Torr, prior to the argon gas flow, to initiate the sputtering. The applied pressure, the argon gas flow rate and the direct current (DC) bias were fixed at 5×10^{-3} Torr, 35 sccm, and 75 V, respectively.

2.4. Fabrication of Ta_2O_5 NTs by anodization

In the present study, to reduce the rate of the anodization reaction and to strengthen the adhesion of the Ta_2O_5 NTs, the HF concentration was kept constant (1% (v/v)). On the other hand, to form

a continuous coating and to prevent severe cracking, a two-step anodization technique was conducted using a DC power source (E3641A, Agilent Technologies, Palo Alto, CA). The as-deposited Ta films were firstly ultrasonicated sequentially in acetone and ethanol for 30 min. The specimens were then connected to the positive terminal (anode) while a platinum foil (15 mm × 15 mm) was used as the negative terminal (cathode) 10 mm away from the anode. The Ta-coated specimens were immersed in an electrolyte of 5% ethylene glycol (EG) dissolved in a 99:1 sulfuric acid (H_2SO_4 98%, Ajax chemicals, Sydney, Australia) and hydrofluoric acid (HF 40%, Ajax chemicals, Sydney, Australia). The anodization experiments were performed at 0 °C at a constant potential of 15 V with different anodization time intervals (0.5, 1, 3, 5, 10, and 20 min). After the anodization, Ta_2O_5 NTs were rinsed with deionized water to remove the excess H_2SO_4 and HF. The Ta_2O_5 NTs were then removed by sonication in deionized water and dehydrated in flowing nitrogen. In order to re-grow the Ta_2O_5 NTs, the anodization procedure was repeated with the same experimental conditions. The anodized specimens were then ultrasonicated in ethanol for 15 min and dried at 100 °C to clean the surface which resulted in a color change from light gray to white. To improve the adhesion of coating, heat treatment was carried out at 450, 500, 550, 750 and 1000 °C for 1 h under atmospheric pressure with a heating/cooling rate of 1 °C min^{-1}. The growth of highly oriented arrays of Ta_2O_5 NTs on Ti64 via the PVD magnetron sputtering, electrochemical anodization and subsequent annealing processes are shown in Scheme 1.

<Scheme 1>

2.5. Characterization

2.5.1. Phase analysis and microstructural characterization

Grazing incidence X-ray diffraction (GIXRD) measurements were performed using a PANalytical Empyrean system (Netherlands) with *Cu–Kα* radiation over a 2θ range from 20° to 80°. The morphology of the coatings was observed on a field emission scanning electron microscopy (FESEM, SU8000, Hitachi, Japan) with an acceleration voltage of 2 kV. To analyze the cross-sectional variation, a destructive technique using a diamond cutting tool was used. Energy-dispersive X-ray spectrometry (EDS) equipped with FESEM was also utilized to examine the elemental compositions.

2.5.2. Adhesion strength

The adhesion strength of the coatings was measured quantitatively using a Micro Materials Nano Test (Wrexham U.K) equipped with a diamond indenter with radius and angle of 25.0 ± 2.0 μm and 90.0 ± 5.0°, respectively. The experiments were performed with a velocity rate of 5 mm s^{-1} and the loading rate gradually increased to 9.2 mN s^{-1}. The scratch tests were repeatedly performed on each sample and the damage profile was investigated under a light optical microscope (Olympus BX61, Tokyo, Japan). Here, the adhesion strength defined as total coating failure. The sample was moved perpendicular to the scratch probe whilst the contact was either held constant or ramped at a user-defined rate. Throughout the test the probe penetration depth and frictional load were continuously monitored. A pre-scratch scan was accomplished using an ultra low contact force in order to assess baseline sample topography. After that, the scratch test was repeated three times within the specified load range using a diamond indenter.

Following the adhesion tests, the obtained data were analyzed by a signal-to-noise (S / N) response method in order to determine the influential process parameters and to optimize the

deposition characteristics. The S / N ratios were calculated using three methods based on the required values (small, large or nominal) to obtain the optimal results. Here, the following equation was used to calculate the S / N ratio (in dB):

$$S/N = -10\log(\frac{1}{n}\sum_{i=1}^{n}\frac{1}{Y_i^2}) \quad \text{(I)}$$

where the term Y is the obtained results and n represents the number of observations.

For further investigation, the scratch hardness test was performed on the as-deposited Ta coating and the 5 min anodized specimen, after annealing at 450 °C for 1 h. This test was executed to measure the resistance of the thin films to permanent deformation under the action of a single point (stylus tip) and involves a different combination of properties of the surface because the indenter, in this case, a diamond stylus, moved tangentially along the surface. The scratch hardness test, is more appropriate technique to measure the damage resistance of a material, like the two-body abrasion. This technique is applicable to a wide range of materials including metals, alloys and some polymers. This test is based on the measurement of the residual scratch width, after the stylus removes to compute the scratch hardness number. Therefore, it reflects the permanent deformation resulting from the scratch and not the instantaneous state of combined elastic and plastic deformation of the surface. Since the state of stress at the stylus tip is a function of contact geometry and applied force, the magnitude of the scratch hardness number is dependent upon both the stylus tip radius and the normal load. The scratch hardness number is calculated by dividing the applied normal force on the stylus by the projected area of the scratch contact, assuming that the hemispherically-tipped stylus produces a groove whose leading surface has a radius of curvature r, the tip radius of the stylus. The projected area of the contact surface is therefore a semi-circle, whose diameter is the

final scratch width. In present work, the critical load is defined at the onset of the coating loss, which is associated with the appearance of the metallic substrate inside the scratch channel. This measurement was accomplished with the help of an optical microscope. The tester was also enabled to obtain the frictional coefficient at the critical load [13,31,32]. The scratch hardness HS_p was estimated following the specification of ASTM G171-03 norm:

$$HS_P = \frac{8P}{\pi w^2} \quad \text{(III)}$$

where HS_p, P and w are the scratch hardness number, normal force and the scratch width, respectively.

2.5.3. Microhardness

The microhardness of the samples were quantified using a Vickers microhardness testing Machine (Mitutoyo-AVK C200-Akashi Corporation, Kanagawa, Japan) by the indentation-strength method at room temperature using an applied load of 98.07 mN and a dwell time of 15 s. Five indentations run per sample were done to determine the average value of the mechanical properties.

2.5.4. Surface wettability

The surface wettability (hydrophilicity) of the specimens was examined by measuring the contact angles of sessile drops of deionized water deposited on each specimen surface. A video-based optical contact angle measuring system (OCA 15EC, DataPhysics Instruments GmbH, Germany) was utilized to inspect the optical wettability. A constant liquid volume of 10 µl was used for the contact angle evaluations of all the specimens using a drop velocity of 2 µl s^{-1} at a temperature of 26±1 °C. The droplet height "*h*" and width "*d*" were measured to calculate the contact angle "θ" as follows [33]:

$$\theta(^{\circ}) = 2\tan^{-1}\left(\frac{2h}{d}\right) \quad \text{(II)}$$

3. Results and discussion

3.1. Mechanism of formation and growth of Ta_2O_5 NTs

A schematic diagram of the anodization process and the different stages of Ta_2O_5 NTs preparation is shown in Scheme 2. The succession of nanotubular oxide layer formation during the anodization of the as-deposited Ta coating could be described as:

(i) Initial barrier layer formation, where there is an exponential decrease in the anodic current density until it reaches a steady state. A decrease in the current is caused by the formation of a compact oxide film that enhances the resistance and decreases the current density. After the development of an initial oxide layer, the O^{2-} or OH^- ions transfer through the oxide layer towards the metal/oxide interface where they react with the Ta metal.

(ii) Uniformly distributed pores formation, where Ta_2O_5 starts to dissolve, leading to the slight increase in the current with time. In this stage, nanopores are generated as a result of random local dissolution of the Ta_2O_5 surface. Fluoride ions are known to chemically attack the Ta_2O_5 and during the anodization, have been found to provide the required dissolution rate of the oxide layer at certain sites, thus creating a porous oxide film. In addition, the applied electrical field ensures that a compact oxide film incessantly restructures at the base of the pores [34].

(iii) Division of interconnected pores into nanotubes and the stabilization of current density. With an adequate applied voltage magnitude, the electric field will be strong enough for the migration of the tantalum ions, leaving behind voids in the interpore areas, which in turn will divide one pore from one another, leading to the development of separate tubes oriented vertically to the substrate [11]. Over stage (iii), nanotubes will form as a result of the simultaneous

growth of voids (regions between pores that are susceptible to field assisted oxidation/dissolution) and pores. It has also been reported that the separation of pores into individual nanotubes may be a consequence of the repulsive forces between the cation vacancies [34,35].

From a chemical aspect, the formation process of the Ta_2O_5 NTs can be also divided into three steps: (i) the migration of Ta^{5+} ions from Ta, (ii) the formation of $Ta_2(OH)_{10}$ and Ta_2O_5 layers on the metal surface; and (iii) the chemical dissolution of Ta_2O_5 to form Ta_2O_5 NTs [36]. However, Ta_2O_5 is soluble in HF, which may result in the etching of the interface between the Ta_2O_5 NTs material and the substrate in step (iii) [34,36]. The etching process leads to the deterioration of the adhesion of Ta_2O_5 NTs, which explains why lower the amount of HF could enhance the connection. The exact reactions are represented in Eqs. 1-10. Besides this, the lower temperature and fast ejection of heat during the Ta anodization could decrease the rate of oxidation reaction which decelerates the volume expansion during the formation of Ta_2O_5 for the sufficient release of the deformational stress. Accordingly, tightly adhered nanotubular arrays could be generated by decreasing the anodization temperature at a reasonable rate to reach a balance between the volume expansion and relieve of the deformational stress [19]. The chemical reactions governing these processes are as follows:

$$10H^+ + 10e^- \rightarrow 5H_2\,(g) \quad (1)$$

$$2Ta \rightarrow 2Ta^{5+} + 10e^- \quad (2)$$

$$2Ta^{5+} + 10H_2O \rightarrow Ta_2(OH)_{10} + 10H^+ \quad (3)$$

$$Ta_2(OH)_{10} \rightarrow Ta_2O_5 + 5H_2O \quad (4)$$

The overall reaction can be written as follows:

$$2Ta + 5H_2O \rightarrow Ta_2O_5 \quad (5)$$

As mentioned above, in acidic solutions, the tantalum oxide-fluoride anions with Ta–O–Ta bridging bonds are formed, after the initial formation of the $[TaOF_5]^{2-}$. The $[TaF_6]^-$ anions are formed in the $[F^-]$ solution, therefore the $[TaF_7]^{2-}$ is the dominant species. The tantalum fluoride species $[TaF_6]^-$ and $[TaF_7]^{2-}$ are successively formed as the result of this mechanism. Throughout these reactions, it should be noted that the successive formation of the tantalum oxide-fluoride/fluoride anions $[TaOF_5]^{2-}$, $[TaF_6]^-$ and $[TaF_7]^{2-}$ occur in higher concentration of HF.

$$HF \leftrightarrow H^+ + F^- \quad (6)$$

$$Ta_2O_5 + 6H^+ + 8F^- \leftrightarrow 2[TaOF_4.H_2O]^- + H_2O \quad (7)$$

$$[TaOF_4]^- + F^- \leftrightarrow [TaOF_5]^{2-} + F^- \quad (8)$$

$$[TaOF_5]^{2-} + F^- \leftrightarrow [TaF_6]^- \quad (9)$$

$$[TaF_6]^- + F^- \leftrightarrow [TaF_7]^{2-} \quad (10)$$

<Scheme 2>

3.2. Phase analysis

Fig. 2 shows the XRD reflections of the substrate (Ti64), the as-sputtered Ta coating and the 5 min anodized sample before and after annealing at 450 °C for 1 h. In accordance with Fig. 2a, the XRD pattern of the substrate displays only the characteristic peaks of Ti (JCPDS#005-0682) located nearly at 2θ = 35.1°, 38.4°, 40.2°, 53.1°, 63.1°, 70.6° and 76.4°, which are related, respectively, to the (1 0 0), (0 0 2), (1 0 1), (1 0 2), (1 1 0), (1 1 2) and (2 0 1) planes. After the PVD coating (Fig. 2b), new diffraction peaks ((1 1 0) plane at 2θ = 38.4° and (2 1 1) plane at 2θ = 69.7°) corresponding to Ta with cubic structure (*Im*-3*m*) and (1 1 0) preferred orientation became apparent in the XRD diffractogram (JCPDS#001-1182). In this case, the characteristic

peaks of Ta_2O_5 are not observed. Depending on the anodization conditions, a variety of ordered and disordered structures can be formed. As shown in Fig. 2c, after 5 min of anodization, some diffraction peaks other than that of Ta are detected, which attributed to the Ta_2O_5 phase with an orthorhombic structure (JCPDS#025-0922). This confirms the formation of Ta_2O_5 during the anodization in H_2SO_4 : HF (99:1) + 5% EG electrolyte with a constant potential of 15 V. It should be mentioned that the fraction of oxide phase and preferred crystal orientation may change after further anodization.

<Fig. 2>

3.3. Microstructural evolution

Given that the microstructural properties and chemical composition of the nanostructured coatings have a significant effect on the biomedical functionality, the microstructural evolution and chemical constituents of the anodized specimens were observed by FESEM and EDS imaging techniques, respectively [37]. As mentioned in the experimental section, the nanostructured coating was firstly synthesized by the anodization of the as-prepared Ta thin film in H_2SO_4 : HF (99:1) + 5% EG electrolyte with a constant potential of 15 V. The obtained coating appeared to have several cracks and tend to peel off or delaminate easily as shown in Fig. 3. The peeling of the oxide film grown under a one-step anodization results in a clean surface of the pure Ta substrate covered with the native oxide [20]. The underlying Ta surface demonstrates a more shallow dimpled morphology after the peeling of the film, formed after the one-step anodization process (Fig. 3b). To overcome the existing problem, various strategies were applied to modify the anodization conditions.

<Fig. 3>

The concentration of HF was kept constant to control the anodization rate and to strengthen the adhesion of the Ta_2O_5 NTs. In addition, to form a continuous coating and to prevent severe cracking, a two-step anodization approach was conducted at constant potential of 15 V at different anodization times. For this purpose, the as-prepared Ta coating was anodized for 20 min at a constant potential of 15 V in the first step. The resulting film could be easily removed from the as-prepared Ta coating by ultrasonication, ensuring a clean Ta surface. This was followed by a second anodization step, to develop a well–adherent Ta_2O_5 NTs with a highly ordered surface topography. Fig. 4 illustrates the FESEM images of a Ta surface after a two-step anodization process, with exposure times ranging from 0.5 to 3 min in H_2SO_4 : HF (99:1) + 5% EG electrolyte, at a constant potential of 15 V. At the brink of the anodization (Fig. 4a to d), some irregular pits were formed due to the localized dissolution of the oxide layer and followed by the pits conversion to larger pores, while most of the areas are still covered with the oxide layer. With extended anodization time to 3 min (Fig. 4e to f), the compact oxide layer disappeared and more uniformly distributed pores were achieved. It is proposed that the pore's ordering is due to the local surface perturbations, where the strain energy increases causing the migration of F^- ions to regions with higher strain energy and more hydrogen ions, in order to maintain the electrical neutrality, leading to the dissolution of the Ta^{5+} ions [35,38]. When the anodization time increased to 5-20 min, clear evolution of nano-porous structure could be observed. From Fig. 4g, well-aligned Ta_2O_5 NTs are formed after 5 min of anodization, where the nanotubes are uniformly distributed over the anodized surface. A higher magnification FESEM image in Fig. 4h reveals that the average inner diameter and tube length are 40 nm and 1 μm, respectively. After 10 min of anodization (Fig. 4i), the top opening of nanotubes are bundled together, which decreases the inner surface area of the nanotubes. In this case, the average inner

diameter and tube length are 36 nm and 2 μm, respectively (Fig. 4j). With the increase of the anodization time to 20 min, the tubes are arranged in tight bundles of ~10 μm length as shown in Fig. 4k and l.

<Fig. 4>

The effect of the anodization time on the thickness of the nanostructured coatings was determined from a cross-sectional view of the FESEM images. Fig. 5a–f shows the FESEM cross-sectional views of the Ta surface after a two-step anodization process with different durations, from 0.5 to 3 min in H_2SO_4 : HF (99:1) + 5% EG electrolyte, at a constant potential of 15 V. From these figures, the Ta_2O_5 NTs are not fully formed between 0.5 to 3 min, this may be the reason of the peeling off or delamination of the coatings. In general, the detachment of the films becomes gradually more difficult as the thickness of the oxide layer increases [20]. Here, the most easily detachable coatings are obtained by growing the oxide for no longer than 3 min, at a constant potential of 15 V. A closer view of the cross sectional images of the 0.5 to 3 min anodized samples shows a heterogeneous structure, where a very porous film rests on a more compact looking oxide with a narrow stripe at the interface to the substrate that likely plays a role in the detachment [20]. In contrast, the anodic oxide films grown for 5 min or more are very stable as shown in Fig. 6. As can be seen, the resulting Ta_2O_5 NTs show a strong adhesion and fully covered the underlying Ta. In a diluted HF solution, the growth rate of nanotubes is significantly lowered, allowing the controlled formation of Ta_2O_5 NTs (~ 1 μm) in a reasonable anodizing time (5 min) as shown in Fig. 6a. With further increase of the anodization time to 10 and 20 min (Fig. 6b and c), the average coating thickness increases to ~ 2 and 4 μm, respectively. From Fig. 6d, the bottom of the oxide nanotubes shows a series of evenly spaced ‘‘bumps” that

signify the pore tips of each individual nanotube. Regarding the thinning of the nanotubes with time, Lockman *et al.* [39] reported that during the first stage of anodization, the field assisted dissolution dominates the chemical dissolution, as the electric field across the electrode is very high. When the anodization progresses and oxide layer thickens, the chemical dissolution will be dominant over the field assisted dissolution. Under such circumstances, chemical dissolution will increase the size and density of the pores. The growth and proliferation of the pores arise by the inward movement at the oxide/metal interface. Accordingly, the discrete hollow-like cylindrical oxide will be formed, which would develop into the nanotubular structure. Given that the oxide layer at the bottom of the pore is exposed to the chemical dissolution, it becomes thinner with time. Besides, if the anodization is performed in concentrated fluoride solution, the dissolution rate would be faster thus the thinning would increase. As the thinning increases, the electric field assisted dissolution will reoccur in this region and thus the pores will penetrate into the sample and the nanotubes grow longer. However, since the voltage is constantly applied, the anodization process would reoccur at the bottom of the pore, developing the nanotubes with a closed bottom.

<Fig. 5>

<Fig. 6>

The relationship between the dimensions of the fabricated Ta_2O_5 NTs and the anodization time, under constant applied anodization voltages is shown in Fig. 7. From this figure, the average length of the nanotube increases with the increase of anodization time to 20 min, but the average inner diameter of the nanotube showed a different trend. The results are consistent with previous studies [35,40]. For the experiments conducted at shorter exposure times, the length of the NTs gradually increased from 73 to 487 nm, for the 0.5 and 3 min anodized samples,

respectively, and thereafter the nanotube lengths steadily approached stable values. After 5 min of anodization, the nanotube lengths reached ~1 μm, and with further increase in the anodization time to 20 min, this value rapidly increased to ~4 μm. It is believed that the electrochemical oxidation rate is likely related to the movement of oxygen-containing anionic species such as O^{2-} and OH^- from the bulk electrolyte to the oxide/metal interface [40]. The mass transport of the oxygen-containing anionic species to the bottom of the nanotube might be hindered with the increase in the nanotube length. When the rates of the electrochemical oxidization of as-prepared Ta coating and the chemical dissolution of Ta_2O_5 NTs reach a dynamic equilibrium, the nanotube lengths approach stable values. From the results of Fig. 7, a small increase in tube diameter is observed with the increase in the anodization time from 0.5 to 3 min. In return, the length of the Ta_2O_5 NTs is strongly affected by the anodization time.

<Fig. 7>

To improve the adhesion of the Ta_2O_5 NTs, heat treatment was performed at a lower heating and cooling rates of 1 °C min^{-1} at 450, 500, 550, 750 and 1000 °C, for 1 h in an atmospheric furnace. The FESEM analysis of the annealed NTs at 450 °C is shown in Fig. 8. The results for the Ta_2O_5 NTs annealed at other temperatures ranging from 500 to 1000 °C are also provided in this figure. As can be seen in Fig. 8a, highly oriented arrays of Ta_2O_5 NTs were formed after the heat treatment at 450 °C for 1 h. Besides, there are no major changes in the microstructural features after annealing at 450 °C. In this case, the length of the NTs and the average inner diameter are ~ 2 μm and 45 nm, respectively (Fig. 8b and c). Similar to the as-prepared NTs, the bottom of the 450 °C annealed sample reveals a series of evenly spaced ‘‘bumps’’ (Fig. 8l). The figure shows that the morphology of the NTs did not collapse and the wall thickness, as well as

the tube diameter did not changed considerably after the heat treatment. It has been reported that the NTs might collapse with specific heat treatment conditions, such as high temperature and extended annealing time [36,41]. In the present case, the surface and the cross-sectional morphologies of the NTs changed after the annealing process at 500 and 550 °C for 1 h (Fig. 8d-i). The FESEM top-view images of the annealed samples at these temperatures show distinct patches of Ta_2O_5 NTs, with the underlying dimpled Ta surface uncovered between the oxide film patches. In accordance with the cross-section image in Fig. 8i, severe oxidation of the barrier layer and minor distortion of the NTs are visible, leading to the shortening of the nanotubes. Any further heat treatment at higher temperatures (typically above 550 °C) will result in the detachment of most of the NTs in an uncontrolled manner as shown in Fig. 8j and k. As shown in Fig. 8j, the nanotubular arrays collapsed at 750 °C. Therefore, the nanotubes will be completely destroyed if the annealing temperature exceeds 1000 °C. Consequently, the nanotubular arrays were converted into a coarse particle structure (Fig. 8k). Similar observations of the collapse of the Ta_2O_5 NTs under heat treatment were previously reported by Gonçalves *et al.* [42]. These findings indicate that temperatures higher than 550 °C are likely to result in structural damage and collapse of the nanotube array structure.

<Fig. 8>

Fig. S1 shows the EDS spectra of the coatings on Ti64 after the two-step anodization process with different durations in H_2SO_4 : HF (99:1) + 5% EG electrolyte, at a constant potential of 15 V. Tantalum and oxygen are the main elements of the coatings from the EDS profiles, and shows the absence of any chemically stable impurity during the anodization process, up to 20 min (Fig. S1a-c). It should be noted that some chemical elements such as

hydrogen or other elements in trace quantities are not detected by the EDS analysis. In fact, the EDS technique is unable to detect the lightest elements, typically below the atomic number of sodium for detectors equipped with a beryllium window. However, polymer-based thin windows allow the detection of light elements and elements present in trace quantities, depending on the instrument and operating conditions. Oxygen composition gradients seem also to appear in some areas of the FESEM images. Thus, to further understand the nature of the NTs, the EDS cross sectional analysis confirmed that the ionic diffusion and the formation of Ta_2O_5 occur all along the tubular structure and not limited to the surface (Fig. S1d).

<Fig. S1>

3.4. Adhesion strength of as-deposited Ta coating and nanotubular arrays

The *S / N* ratio is a measurement to determine the degree of predictable performance of a process and to decrease the process sensitivity to noise factors. The *S / N* ratios calculated for the adhesion strength are presented in Tables 3, whereas the corresponding *S / N* values for the coating parameters are provided in Table 4 and Fig. 9. According to ''*the higher the better*'' criteria, the higher *S / N* ratios indicate more desirable responses, resulting in lower negative effects caused by the noise in the machine setup. Therefore, a DC power of 350 W, temperature of 250 °C and a deposition time of 6 h were considered as the optimal conditions for attaining the highest adhesion strength. In order to validate this finding, a confirmation study was performed with these optimal parameters. The adhesion strength achieved in this experiment was 2154 mN, which indicates a 19.8 % improvement compared to the maximum adhesion strength value achieved from the experimental conditions shown in Table 3.

<Table 3>

<Table 4>

<Fig. 9>

Fig. 10 illustrates the top-view and cross-sectional FESEM images of the Ta thin films under different PVD conditions. The FESEM images indicate a lamellar coating structure which became denser as the DC power increased from 250 to 350 W. Furthermore, the process duration exhibited a positive effect on the coating thickness. Therefore, the increased DC power and process duration resulted in higher a coating compaction and density along with an improved coating adhesion, which subsequently increased the surface adhesion. Such improved adhesion could arise from the higher available energy for the film growth. With increasing the DC power, the ionized particles become more energetic, resulting in a decreased distance between the energized atoms and increased sputtering rate. This shows that the energetic atoms with higher motilities are preferably deposited onto the lower-energy surfaces, causing greater coating density and adhesiveness [43]. Accordingly, the combination of a DC power of 350 W, temperature of 250 °C and a deposition time of 6 h are the optimal operating conditions for obtaining the highest adhesion strength.

<Fig. 10>

On account of the long periods of presence in the living body, the main features of the implant materials are the stability and durability. Accordingly, improving the adhesion strength between the coating layers and implant is vital [44]. Fig. 11 illustrates the optical micrograph of the scratch track and profiles of depth, load, friction and coefficient of friction (COF) *vs.* scan distance for the optimized sample. Here, the scratch direction was from left to right. As shown in

Fig. 11a, the scratch length and the failure point of the as-deposited Ta layer were 1127 and 887 μm, respectively. The critical loads (Le-p, Lc_1, Lc_2 and Lc_3) delineated by a drastic alteration of depth vs. distance profile, where Le-p refers to an elastic-to-plastic transition and cohesive failure (Fig. 11b). Moreover, the L_{c1}, L_{c2}, and L_{c3} refers to a lower critical load, with the initiation of a parallel and edge cracking, failure or upper critical load by partial coating delamination along with a subsequent intermittent substrate exposure, and total coating failure by complete exposure of the surface material, respectively [44]. From Fig. 11c, the optimized sample under the applied load gave an adhesion strength of 2154 mN. The friction can also be denoted as the resistance tangential force to a relative motion between two surfaces in contact. Hence, during the scratch adhesion test, the friction and coefficient of friction were calculated and plotted *vs.* the scratch length. According to Fig. 11d and e, the calculated friction and COF for the optimized sample with the highest adhesion were 1356 mN and 0.59, respectively.

<Fig. 11>

Fig. 12 displays the different types of failure mode during the scratch test of the Ta coating on the substrate. The as-deposited coating process began to fail in the advent of some cracking on the trackside. This critical load was recorded as L_{c1}, which was followed by a mild tensile cracking during the scratch path. By gradually increasing of the load amount, delamination occurred on the trackside, and the load value was recorded as L_{c2}. With further increase in the load rate, the cracking and delamination became dominant and the spacing between the tensile cracks areas became smaller than before, until the coating was delaminated (recorded as L_{c3}). When the load value increased continuously, the spallation around the trackside substituted the

trackside delamination and the width of the scratch became constant, as shown in Fig. 12. A similar trend was observed in previous studies [13, 45-47].

<Fig. 12>

As mentioned earlier, depending on the application, enhancement of the adhesion strength between coating layers and implant materials is very important. In reality, the adhesion of a coating to a substrate and the integrity of the substrate/coating interface are always connected to the performance and reliability of any coated surface [43]. Fig. 13 illustrates the graphs of depth, load, friction and COF versus the distance, as well as the failure points of the 5 min anodized specimen after annealing at 450 °C for 1 h during the scratch test. The critical loads were defined on the basis of the load-displacement graph. It should be noted that the scratch direction was from left to right, as shown in Fig. 13a. As can be seen, the total scratch length of the 450 °C annealed sample is 1024 μm, against which the coating total failure was detected at a distance 863 μm. In addition, the adhesion strength of the coating increased to 2301 mN after the heat treatment. From Fig. 13d and e, the calculated friction and COF of the annealed coating decreased to 1056 mN and 0.56, respectively. Concerning the scratch depth (~ 6 μm) of the anodized sample after annealing, this behavior could be due to the complementary effect of the Ta coating as an intermediate layer. In fact, the observed value of the penetration depth is related to Ta/Ta_2O_5 NTs layer, where the inter diffusion of Ta between substrate and nanotubular configuration has contributed to strong interlock for higher adhesion strength.

According to Figs. 11 and 13, the scratch width of the annealed sample is narrower than the as-deposited Ta coating and consequently the scratch hardness of the annealed coating (2.9 GPa)

is higher than that of the as-deposited thin film (1.8 GPa). These findings imply that the subsequent annealing process may have a dramatic impact on the adhesion of the thin films.

<Fig. 13>

3.5. Vickers microhardness

To control the quality of the coatings, Vickers microhardness test was conducted. Fig. S2 shows the disparity in the Vickers hardness of the substrate, as-deposited Ta layer and 5 min anodized sample before and after the annealing process at 450 °C for 1 h. The microhardness of the substrate and the as-sputtered Ta layer was 263 and 290 HV, respectively, and rose to 297 HV after 5 min of anodization. This effect can be linked to the presence of the nanotubular arrays which can improve the mechanical properties of the material. During the annealing process at 450 °C for 1 h, a substantial decrease in the amount of chemisorbed water occurred during annealing of the anodized specimens which in turn led to the densification of the nanotubes and thus resulted in an increase in surface hardness to 356 HV as reported previously [48,49]. This result is entirely consistent with the FESEM observations, where a highly oriented arrays of Ta_2O_5 NTs was detected after annealing at 450 °C for 1 h. Accordingly, the heat treatment at 450 °C at atmospheric pressure is the most favorable condition for the subsequent annealing of the Ta_2O_5 NTs.

<Fig. S2>

3.6. Surface wettability of nanotubular arrays

In general, wettability is the tendency of a fluid to spread on, or adhere to, a solid surface in the presence of other immiscible fluids. In reality, wettability refers to the interaction between

the fluid and solid phases and is defined by the contact angle of the fluid with the solid phase. The degree of wetting (wettability) is determined by a force balance between the adhesive and cohesive forces, where wetting deals with the three states of matter: gas, liquid and solid. Due to the appearance of a wide range of nanomaterials in the recent years, this technique is gaining popularity in nanotechnology and nanoscience investigations [50,51]. The contact angle values indicate whether the surface is hydrophilic or hydrophobic. Fig. 14 displays the variation of the deionized water contact angle of the substrate, as-deposited Ta layer and 5 min anodized sample before and after the annealing process at 450 °C for 1 h. It is clear that the 5 min anodization and subsequent annealing at 450 °C play an important role in determining the surface wettability of the material. According to Fig. 14a and b, the substrate and the as-sputtered Ta layer show a contact angle value of 72.8° and 54.8°, respectively. After 5 min of anodization, this value decreases to 37.7°, which suggests that the wetting of the surface is very favorable, where the hydrophilic properties of the substrate has improved after 5 min of anodization (Fig. 14c). So it can be concluded that the nanotubular configuration can increase the hydrophilicity of the titanium implant surfaces, thereby the cell attachment, extension and spreading, as well as cytoskeletal organization can improve the biomedical functionality [48,52]. As shown in Fig. 14d, an improvement in the surface hydrophilicity (28.1°) was observed after annealing at 450 °C, which can be interpreted by the superficial cleanliness, crystal structure, oxygen vacancy defects and surface morphology [53]. It has been reported that the protein activities on the surface of the orthopedic implants is dependent on the surface properties, especially on adsorption and adhesion [54]. The implant surface wettability also influences the cell behavior in the initial osseointegration process, whereas the osseointegration mechanism begins when the implant is in contact with the blood. In the case of hydrophobic surfaces, the signs of the antibodies decreases

the cell adsorption. On the contrary, in the hydrophilic surfaces, the signs of the antibodies are predominant and adsorption is stimulated [55]. Therefore, the surface modification by Ta coating and subsequent anodization and annealing can change the composition, topography, roughness and wettability and when in connection with the cell behavior, it can modify in the initial mechanisms of osseointegration.

<Fig. 14>

4. Conclusion

To sum up, the surface modification of Ti–6Al–4V alloy was performed by Ta PVD magnetron sputtering with subsequent electrochemical anodization of the as-sputtered coating. An optimization study on the PVD magnetron sputtering conditions was done using the Taguchi method. Then, the Ta_2O_5 NTs were grown by a two-step anodization technique in H_2SO_4 : HF (99:1) + 5% EG electrolyte at a constant potential of 15 V. To improve the adhesion of coating, thermal annealing process was also done in the temperature range between 450 to 1000 °C for 1 h. Based on the FESEM observations, Ta_2O_5 NTs were not fully formed between 0.5 to 3 min. Conversely, the anodic oxide films grown for 5 min showed strong adhesion and full coverage of the underlying Ta. The average length of the nanotube increased to ~4 μm with the increase of the anodization time to 20 min, but the average inner diameter of the nanotube showed a different trend. The results showed that heat treatment at 450 °C in atmospheric pressure was the most favorable for the subsequent annealing of the Ta_2O_5 NTs, where a maximum surface hardness (356 HV) and adhesion strength (2301 mN) were achieved. Increasing the annealing temperature to 1000 °C resulted in the complete collapse of the nanotubes. Compared to the

untreated sample and as-deposited Ta coating, the 450 °C annealed coating showed the highest wettability.

Acknowledgement

The authors would like to acknowledge the University of Malaya for providing the necessary facilities and resources for this research. This research was fully founded by the Ministry of Higher Education, Malaysia with the high impact research grant numbers of UM.C/HIR/MOHE/ENG/27. The authors also wish to thank the University of Malaya grant number RP038C 15HTM and PG084-2013A. The authors are also grateful to Research Affairs of Islamic Azad University, Najafabad Branch for supporting of this research.

References

[1] X. Liu, P.K. Chu and C. Ding, *Mater. Sci. Eng. R*, 2004, **47**, 49–121.
[2] H.J. Rack and J.I. Qazi, *Mater. Sci. Eng. C*, 2006, **26**, 1269–1277.
[3] J.D. Bobyn, R.M. Pilliar, H.U. Cameron and G.C. Weatherly, *Clin. Orthop.*, 1980, **150**, 263–270.
[4] G. Wu, P. Li, H. Feng, X. Zhang and P.K. Chu, *J. Mater. Chem. B*, 2015, **3**, 2024–2042.
[5] D. Tang, R.S. Tare, L.Y. Yang, D.F. Williams, K.L. Ou and R.O.C. Oreffo, *Biomaterials*, 2016, **83**, 363–382.
[6] J. Raphel, M. Holodniy, S.B. Goodman and S.C. Heilshorn, *Biomaterials*, 2016, **84**, 301–314.
[7] V.K. Balla, S. Banerjee, S. Bose and A. Bandyopadhyay, *Acta Biomater.*, 2010, **6**, 2329–2334.
[8] C. Balagna, M. Faga and S. Spriano, *Materials Science and Engineering: C*, 2012, **32**, 887–895.
[9] C. J. Frandsen, K. S. Brammer, K. Noh, G. Johnston and S. Jin, *Materials Science and Engineering: C*, 2014, **37**, 332–341.
[10] B. Rahmati, A.A. Sarhan, E. Zalnezhad, Z. Kamiab, A. Dabbagh, D. Choudhury and W. Abas, *Ceram. Int.*, 2016, **42**, 466–480.
[11] N.K. Allam, X.J. Feng and C.A. Grimes, *Chemistry of Materials*, 2008, **20**, 6477–6481.
[12] T. Ruckh, J. R. Porter, N. K. Allam, X. Feng, C. A. Grimes and K. C. Popat, *Nanotechnology*, 2009, **20**, 045102.
[13] M. Sarraf, E. Zalnezhad, A. Bushroa, A. Hamouda, S. Baradaran, B. Nasiri-Tabrizi and A. Rafieerad, *Appl. Surf. Sci.*, 2014, **321**, 511–519.
[14] W. M. Yang, Y. W. Liu, Q. Zhang, Y. X. Leng, H. F. Zhou, P. Yang, J. Y. Chen and N. Huang, *Surf. Coat. Tech.*, 2007, **201**, 8062–8065.

[15] L. Chongyan, Z. Xu, Z. Rong, Z. Huixing and W. Xianying, *Rare Metal Mat. Eng.*, 2008, **37**, 556–560.
[16] N. Wang, H. Li, J. Wang, S. Chen, Y. Ma and Z. Zhang, *ACS Appl. Mater. Interfaces*, 2012, **4**, 4516–4523.
[17] S.M. Jafari, B. Bender, C. Coyle, J. Parvizi, P.F. Sharkey and W.J. Hozack, *Clin. Orthop. Relat. Res.*, 2010, **468**, 459–465.
[18] K.B. Sagomonyants, M. Hakim-Zargar, A. Jhaveri, M.S. Aronow and G. Gronowicz, *J. Orthop. Res.*, 2011, **29**, 609–616.
[19] P. Zhang, T. Wang, J. Zhang, X. Chang and J. Gong, *Nanoscale*, 2015, **7**, 13153–13158.
[20] S. Singh, M. T. Greiner and P. Kruse, *Nano lett.*, 2007, **7**, 2676–2683.
[21] C. Horwood, H. El-Sayed and V. Birss, *Electrochim. Acta*, 2014, **132**, 91–97.
[22] R.V. Gonçalves, P. Migowski, H. Wender, D. Eberhardt, D.E. Weibel, F.V.C. Sonaglio, M.J. Zapata, J. Dupont, A.F. Feil and S.R. Teixeira, *J. Phys. Chem. C*, 2012, **116**, 14022–14030.
[23] Z. Su, S. Grigorescu, L. Wang, K. Lee and P. Schmuki, *Electrochem. Commun.*, 2015, **50**, 15–19.
[24] S. Banerjee, S.K. Mohapatra and M. Misra, *Chem. Commun.*, 2009, 7137–7139.
[25] J.E. Barton, C.L. Stender, P. Li and T.W. Odom, *J. Mater. Chem.*, 2009, **19**, 4896–4898.
[26] C.A. Horwood, H. El-Sayed and V.I. Birss, 219th ECS Meeting, 2011.
[27] H.A. El-Sayed and V.I. Birss, *Nano lett.*, 2009, **9**, 1350–1355.
[28] H. El-Sayed, S. Singh and P. Kruse, *J. Electrochem. Soc.*, 2007, **154**, C728–C732.
[29] I.V. Sieber and P. Schmuki, *J. Electrochem. Soc.*, 2005, **152**, C639–C644.
[30] J. Ghani, I. Choudhury and H. Hassan, *J. Mater. Process. Tech.*, 2004, **145**, 84–92.
[31] ASTM G171-03, Standard Test Method for Scratch Hardness of Materials Using a Diamond Stylus, ASTM International, West Conshohocken, PA, 2003, www.astm.org
[32] R. Jaworski, L. Pawlowski, F. Roudet, S. Kozerski and F. Petit, *Surf. Coat. Tech.*, 2008, **202**, 2644–2653.
[33] C.N. Elias, Y. Oshida, J.H.C. Lima and C.A. Muller, *J. Mech. Behav. Biomed. Mater.*, 2008, **1**, 234–242.
[34] H. A. El-Sayed and V. I. Birss, *Nanoscale*, 2010, **2**, 793-798.
[35] G. A. Crawford, N. Chawla, K. Das, S. Bose and A. Bandyopadhyay, *Acta Biomater.*, 2007, **3**, 359–367.
[36] A. E. R. Mohamed and S. Rohani, *Energy & Environmental Science*, 2011, **4**, 1065–1086.
[37] A. R. Rafieerad, A. R. Bushroa, B. Nasiri-Tabrizi, J. Vadivelu, S. Baradaran, E. Zalnezhad and A. Amiri, *RSC Adv.*, 2016, **6**, 10527–10540.
[38] S. Sobieszczyk, *Adv. Mater. Sci.*, 2009, **9**, 25–41.
[39] Z. Lockman, S. Sreekantan, S. Ismail, L. Schmidt-Mende and J. L. MacManus-Driscoll, *J. Alloy. Compd.*, 2010, **503**, 359–364.
[40] Y. Ku, Z-R. Fan, Y-C. Chou and W-Y. Wang, *J. Electrochem. Soc.*, 2010, **157**, H671–H675.
[41] A. Ghicov, H. Tsuchiya, J. M. Macak and P. Schmuki, *Phys. Status Solidi A*, 2006, **203**, R28–R30.
[42] R.V. Gonçalves, R. Wojcieszak, P.M. Uberman, S.R. Teixeira and L.M. Rossi, *Phys. Chem. Chem. Phys.*, 2014, **16**, 5755–5762.

[43] S. Baradaran, W. Basirun, E. Zalnezhad, M. Hamdi, A. A. Sarhan and Y. Alias, *J. Mech. Behav. Biomed. Mater.*, 2013, **20**, 272–282.
[44] A.P. Tomsia, E. Saiz, J. Song and C.R. Bertozzi, *Adv. Eng. Mater.*, 2005, **7**, 999–1004.
[45] K. Singh, N. Krishnamurthy and A. Suri, *Tribol. Int.*, 2012, **50**, 16–25.
[46] J. A. Toque, M. K. Herliansyah, M. Hamdi, A. Ide-Ektessabi and I. Sopyan, *J. Mech. Behav. Biomed. Mater.*, 2010, **3**, 324–330.
[47] A. Bushroa, H. Masjuki, M. Muhamad and B. Beake, *Surf. Coat. Tech*., 2011, **206**, 1837–1844.
[48] H. Yaghoubi, N. Taghavinia, E. K. Alamdari and A. A. Volinsky, *ACS applied materials & interfaces*, 2010, **2**, 2629–2636.
[49] M. Sarraf, E. Zalnezhad, A. Bushroa, A. Hamouda, A. Rafieerad and B. Nasiri-Tabrizi, *Ceramics International*, 2015, **41**, 7952–7962.
[50] A.R. Rafieerad, A.R. Bushroa, B. Nasiri-Tabrizi, J. Vadivelu, S. Baradaran, M. Mesbah and M. Akhtari Zavareh, *Mater. Design*, 2016, **103**, 10–24.
[51] J. Rafiee, X. Mi, H. Gullapalli, A.V. Thomas, F. Yavari, Y. Shi, P.M. Ajayan, N.A. Koratkar, *Nature Mater.*, 2012, **11**, 217–222.
[52] Z. He, J. Xiao, F. Xia, K. Kajiyoshi, C. Samart and H. Zhang, *Appl. Surf. Sci.*, 2014, **313**, 633–639.
[53] L. Yang, M. Zhang, S. Shi, J. Lv, X. Song, G. He and Z. Sun, *Nanoscale Res. Lett.*, 2014, **9**, 621.
[54] C.N. Elias, Y. Oshida, J.H.C. Lima and C.A. Muller, *J. Mech. Behav. Biomed. Mater.*, 2008, **1**, 234–42.
[55] J.M. Macak, H. Tsuchiya, A. Ghicov, K. Yasuda, R. Hahn, S. Bauer and P. Schmuki, *Curr. Opinion Solid State Mater. Sci.*, 2007, **11**, 3–18.

List of Figures Caption

Scheme 1 The growth of the highly oriented arrays of Ta_2O_5 NTs on Ti64 derived by PVD magnetron sputtering, electrochemical anodization and subsequent annealing.

Scheme 2 A schematic diagram of the anodization process and the different stages of Ta_2O_5 NTs preparation.

Fig. 1 EDS analysis of the substrate (Ti–6Al–4V).

Fig. 2 XRD reflections of the (a) substrate, (b) as-sputtered Ta coating, and (c) 5 min anodized sample.

Fig. 3 Peeling of an oxide film grown with a one-step anodization process.

Fig. 4 FESEM images of a Ta surface after the two-step anodization process with exposure times from 0.5 to 20 min in H_2SO_4 : HF (99:1) + 5% EG electrolyte at a constant potential of 15 V; (a,b) 0.5, (c,d) 1, (e,f) 3, (g,h) 5, (i,j) 10, and (k,l) 20 min.

Fig. 5 FE-SEM cross-sectional views of the Ta surface after the two-step anodization process with different durations from 0.5 to 3 min in H_2SO_4 : HF (99:1) + 5% EG electrolyte at a constant potential of 15 V; (a,b) 0.5, (c,d) 1, and (e,f) 3 min.

Fig. 6 FE-SEM cross-sectional views of the Ta surface after a two-step anodization with different durations ranging from 5 to 20 min in H_2SO_4 : HF (99:1) + 5% EG electrolyte with a constant potential of 15 V; (a) 5, (b) 10, and (c) 20 min as well as (d) bottom of the oxide nanotubes.

Fig. 7 The relationship between the dimensions of the fabricated Ta_2O_5 NTs and anodization time at constant anodization voltages.

Fig. 8 FESEM images (top- and cross-sectional views) after annealing at (a–c) 450, (d–f) 500, (g–i) 550, (j) 750, and (k) 1000 °C for 1 h; (l) FESEM image (bottom view) of the Ta_2O_5 NTs annealed at 450 °C for 1 h.

Fig. 9 The *S / N* response of (a) time, (b) temperature, and (c) DC power for adhesion strengh.

Fig. 10 Top-view and cross-sectional FESEM images of the as-deposited Ta thin films with different operating conditions; (a,d) 250 W–300 °C–6h, (b,e) 300 W–250 °C–6h and (c,f) 350 W–250 °C–6h.

Fig. 11 (a) The optical micrograph of the scratch track and (b) profiles of depth, (c) load, (d) friction, and (e) coefficient of friction *vs.* scan distance for the optimized sample.

Fig. 12 Failure mode of the tantalum coating on Ti–6Al–4V during the scratch test.

Fig. 13 (a) The optical micrograph of the scratch track and (b) graphs of depth, (c) load, (d) friction and (e) COF versus distance as well as the failure points of the 5 min anodized specimen after annealing at 450 °C for 1 h.

Fig. 14 The variation of the deionized water contact angle of the (a) substrate, (b) as-deposited Ta layer and 5 min anodized sample (c) before and (d) after annealing at 450 °C for 1 h.

List of Tables Caption

Table 1 Different protocols used in the synthesis of Ta_2O_5 NTs via the anodization technique.

Table 2 The control parameters and their corresponding levels used in these experiments.

Table 3 The measured scratch force and calculated *S / N* ratio.

Table 4 The *S / N* response values obtained from the adhesion strength.

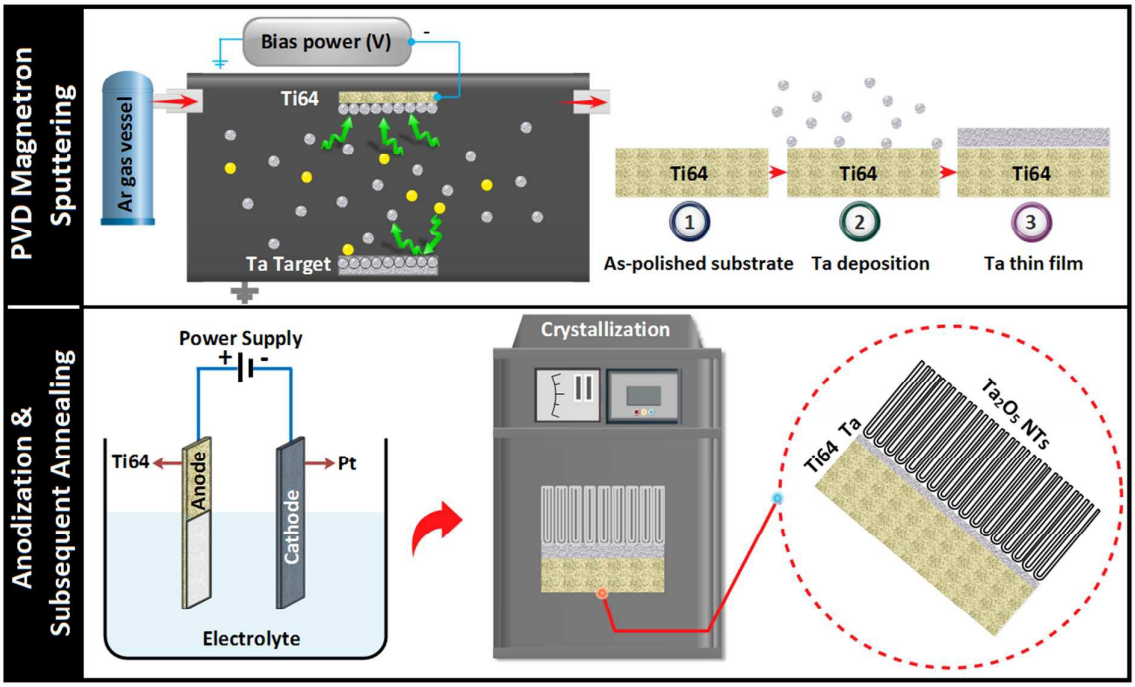

Scheme 1

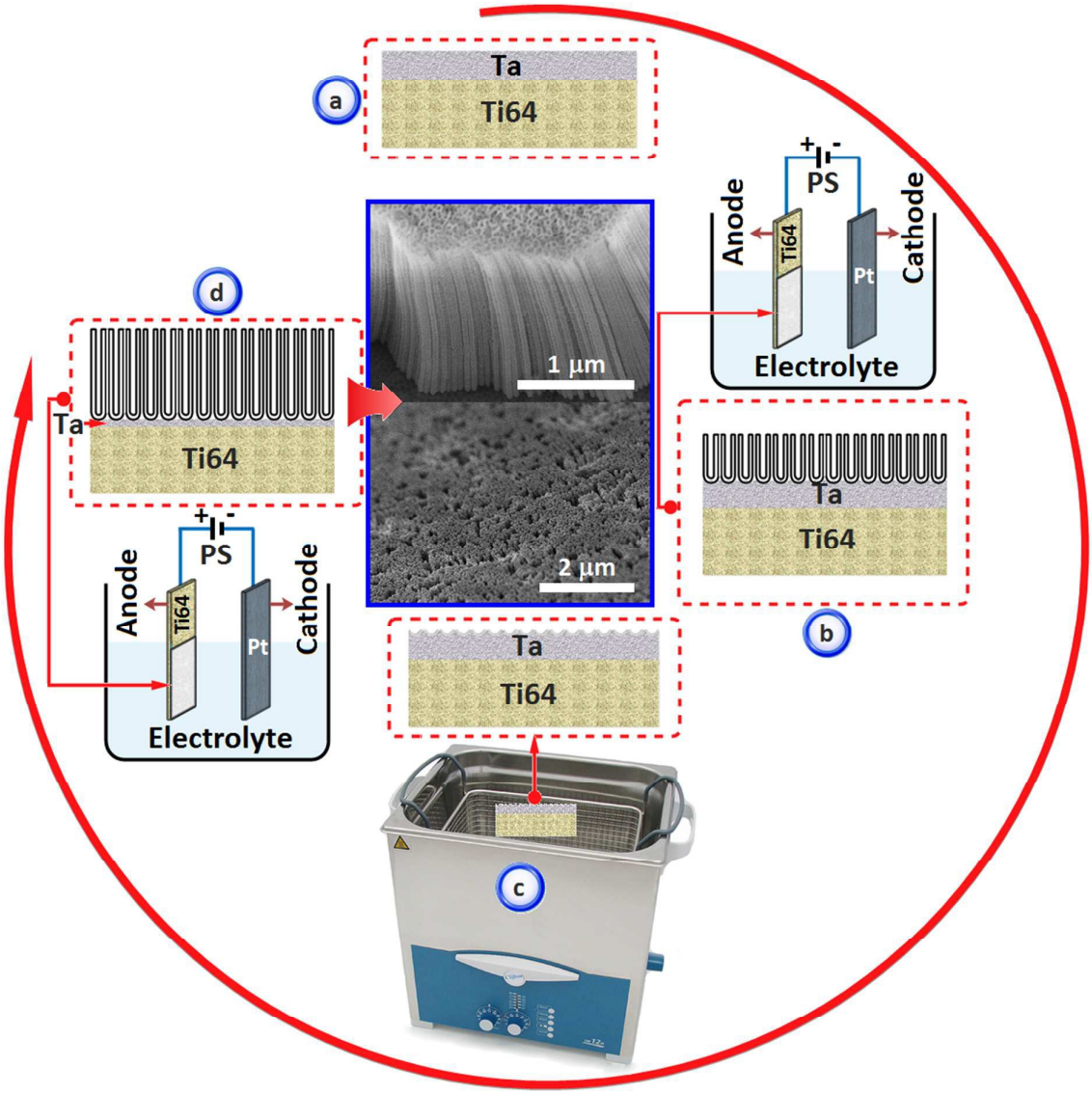

Scheme 2

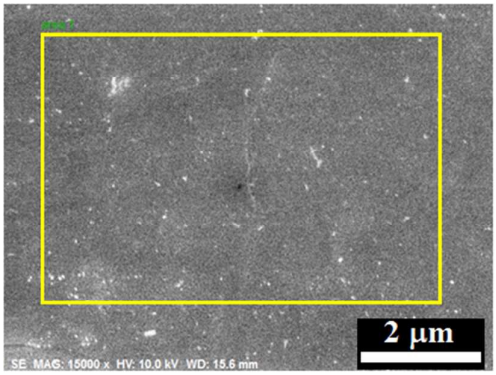

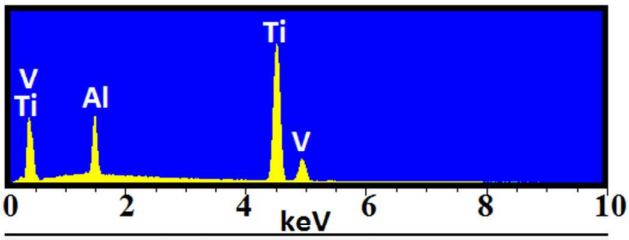

Element	Series	C (wt%)	C (at%)
Al	K-series	5.29	9.03
Ti	K-series	91.13	87.72
V	K-series	3.59	3.24

Fig. 1

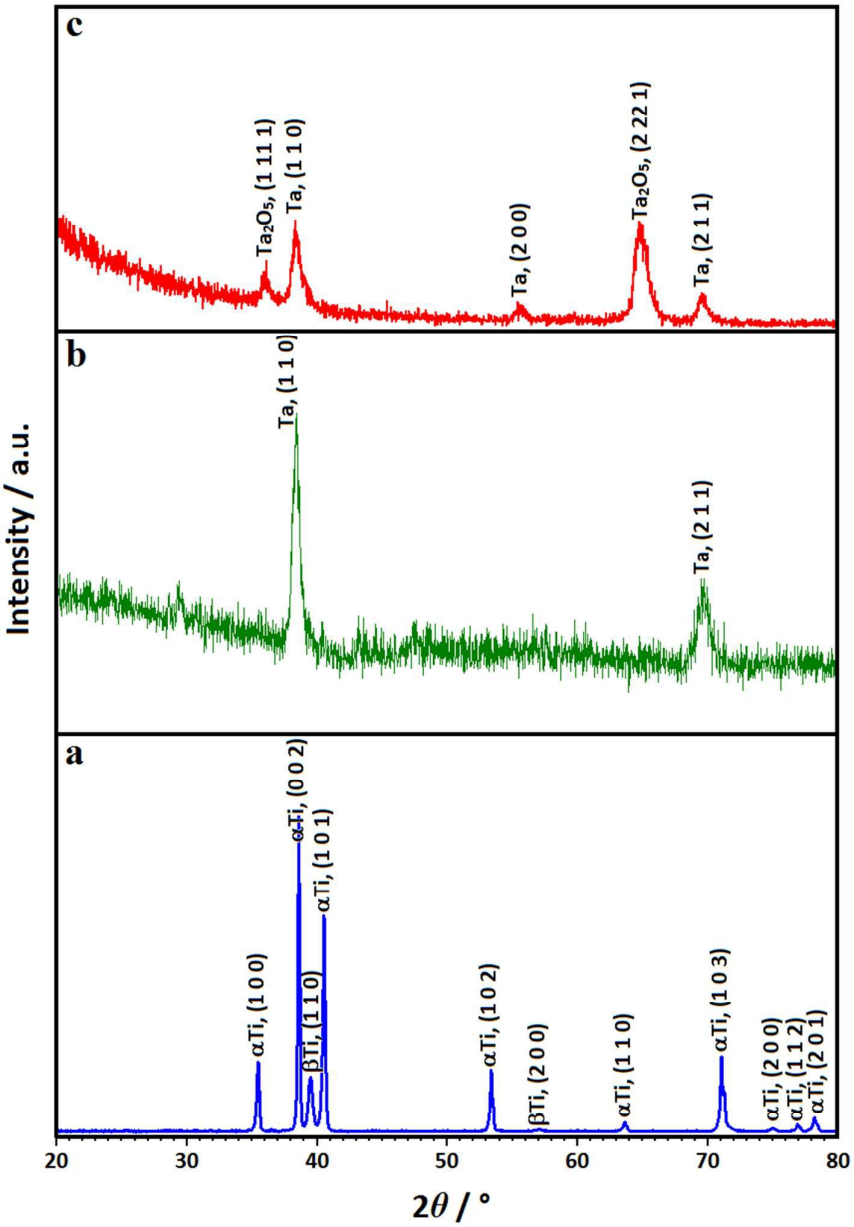

Fig. 2

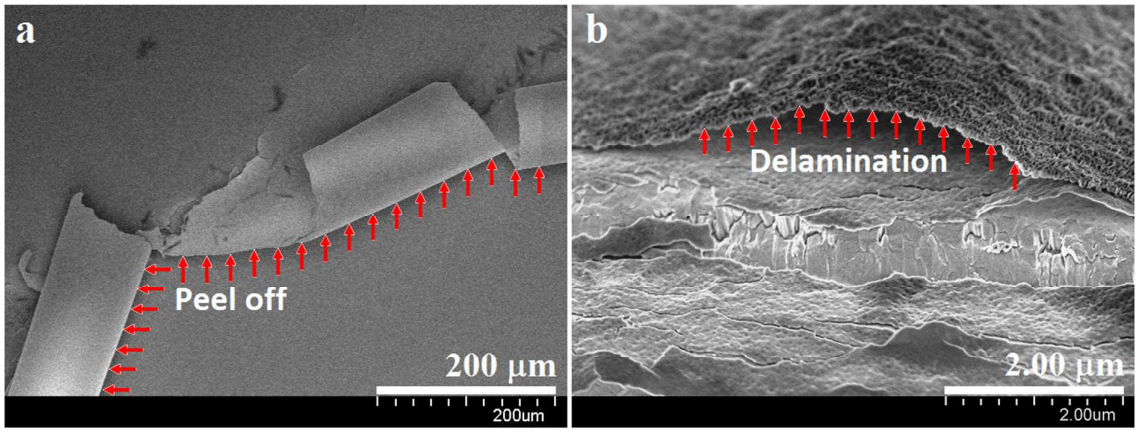

Fig. 3

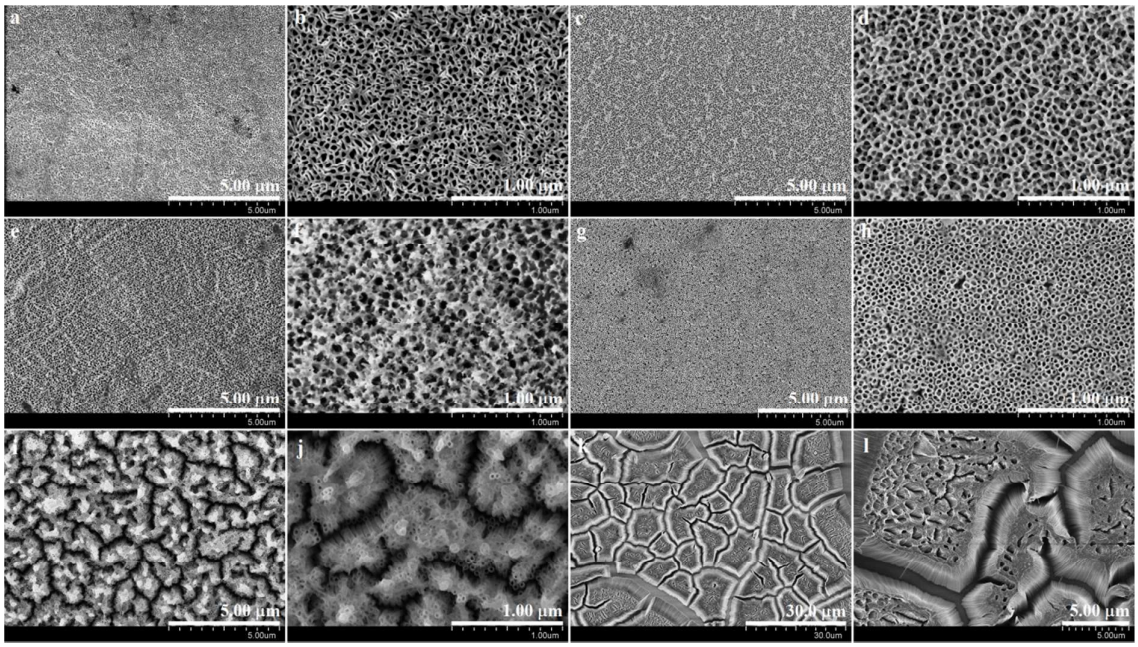

Fig. 4

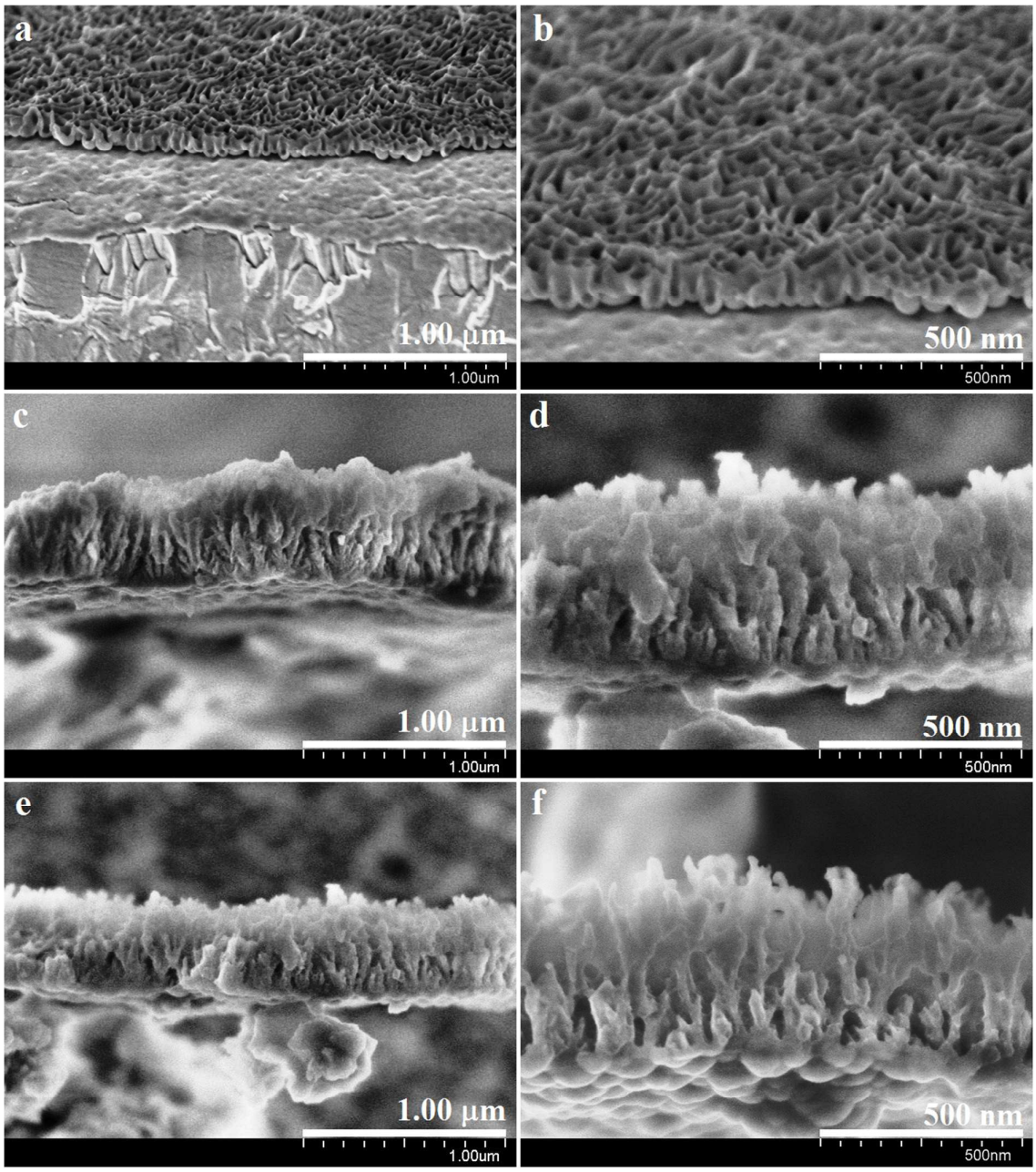

Fig. 5

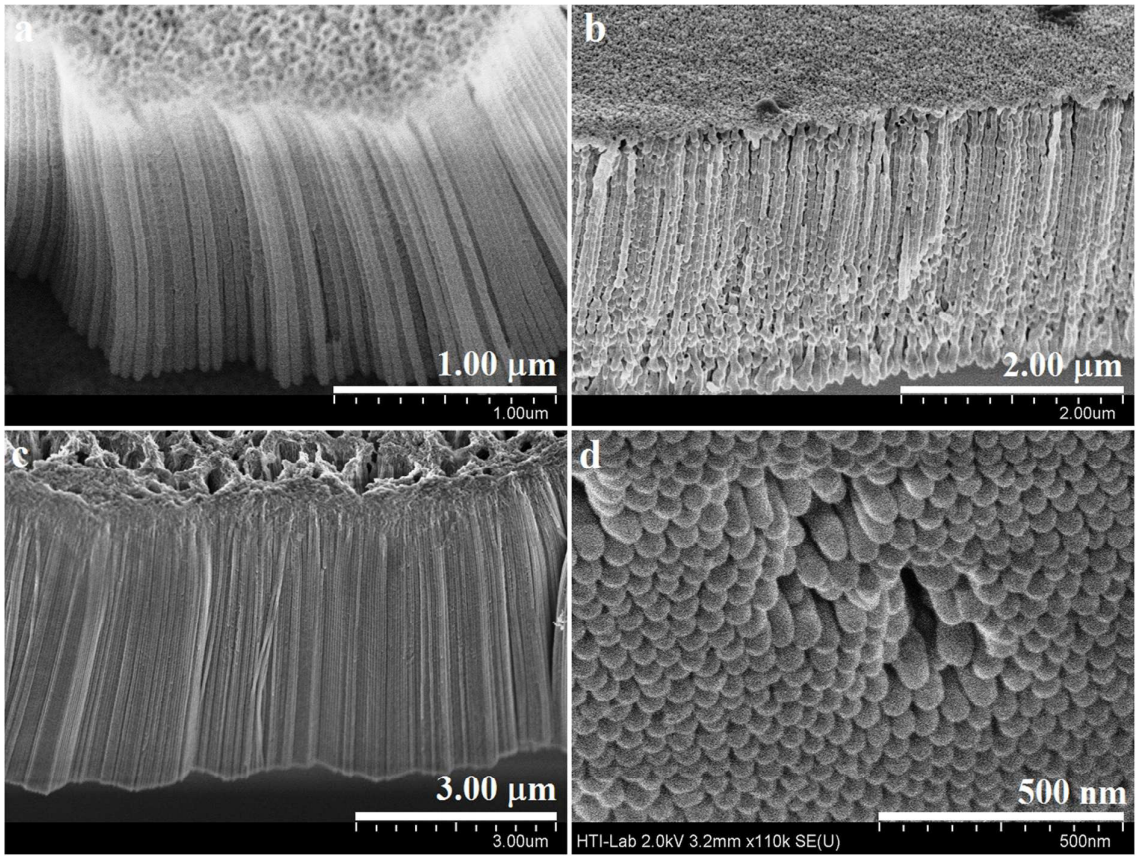

Fig. 6

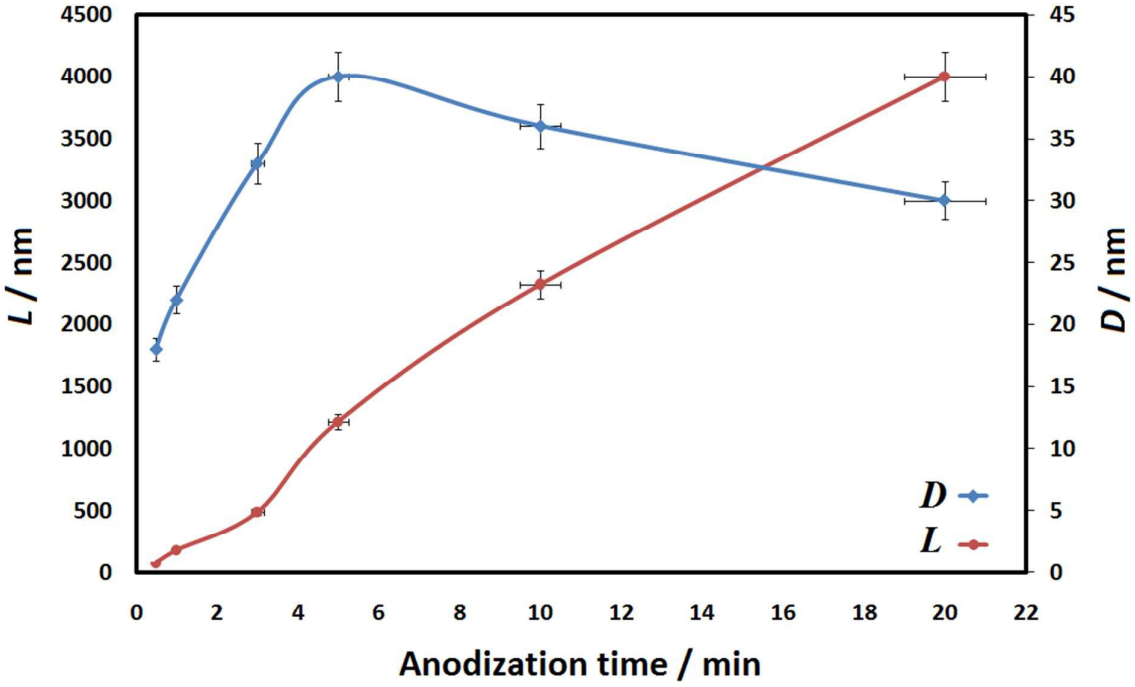

Fig. 7

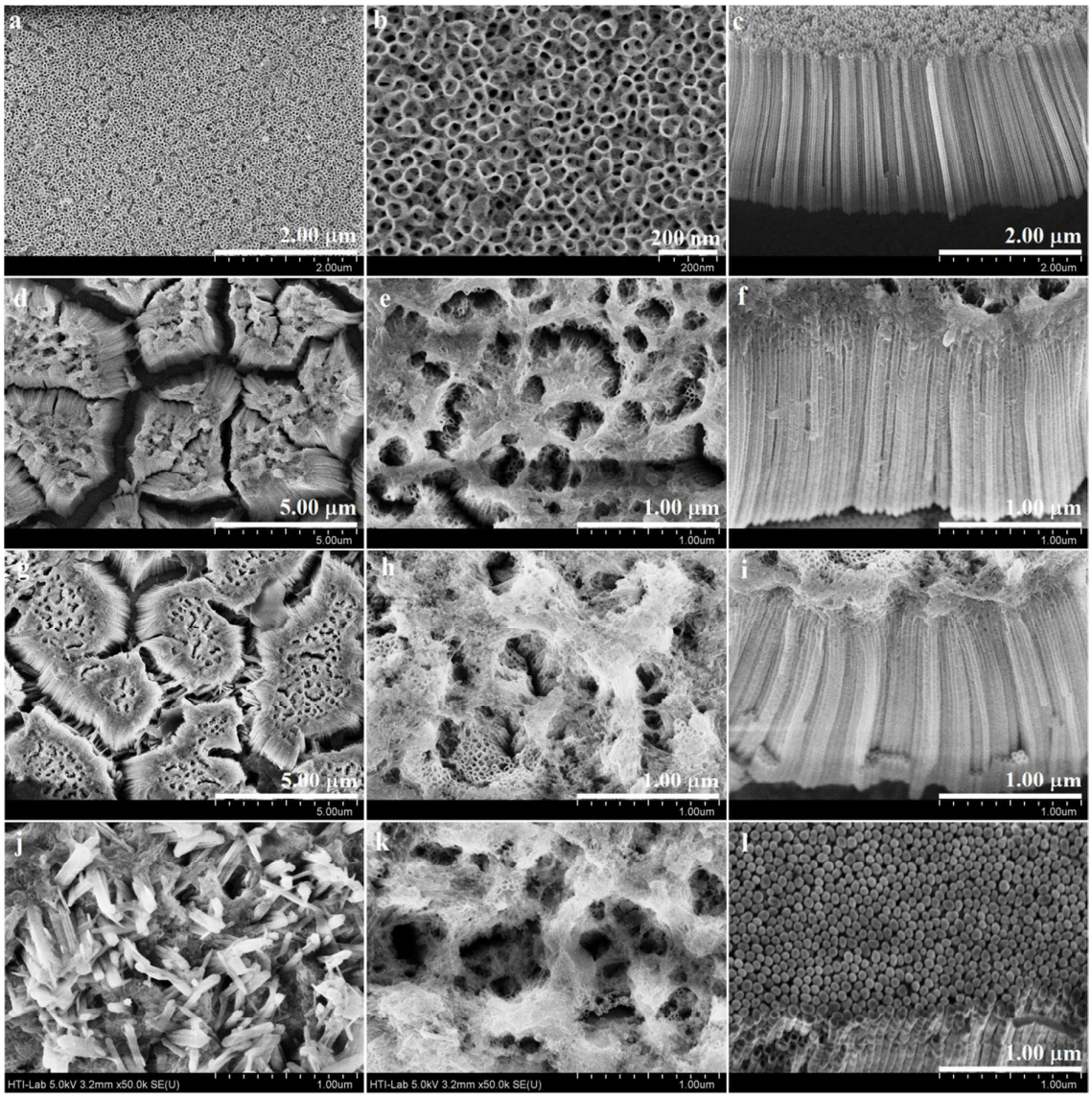

Fig. 8

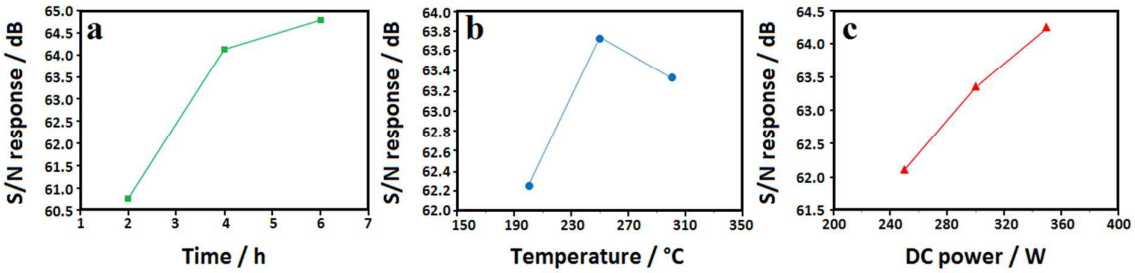

Fig. 9

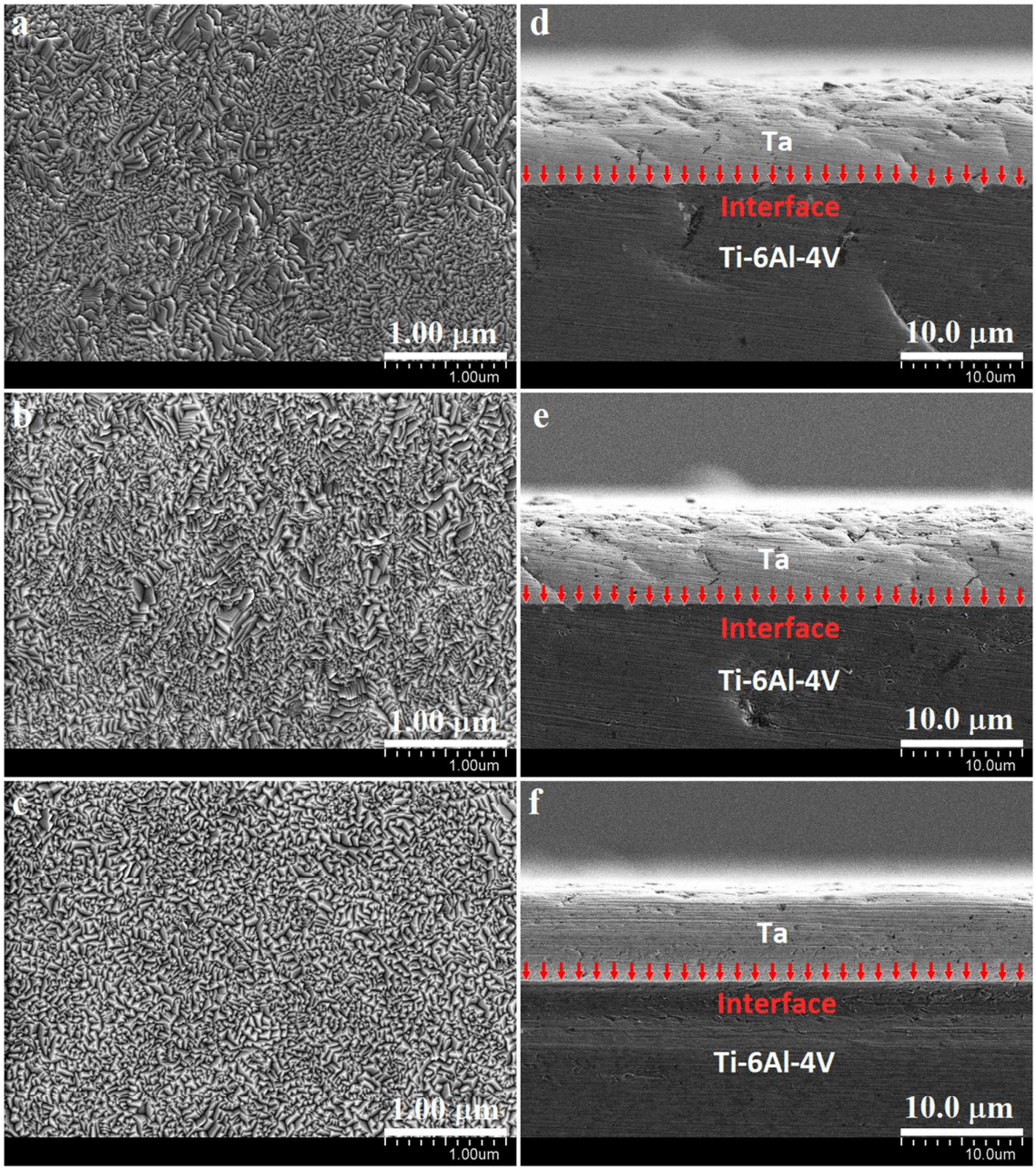

Fig. 10

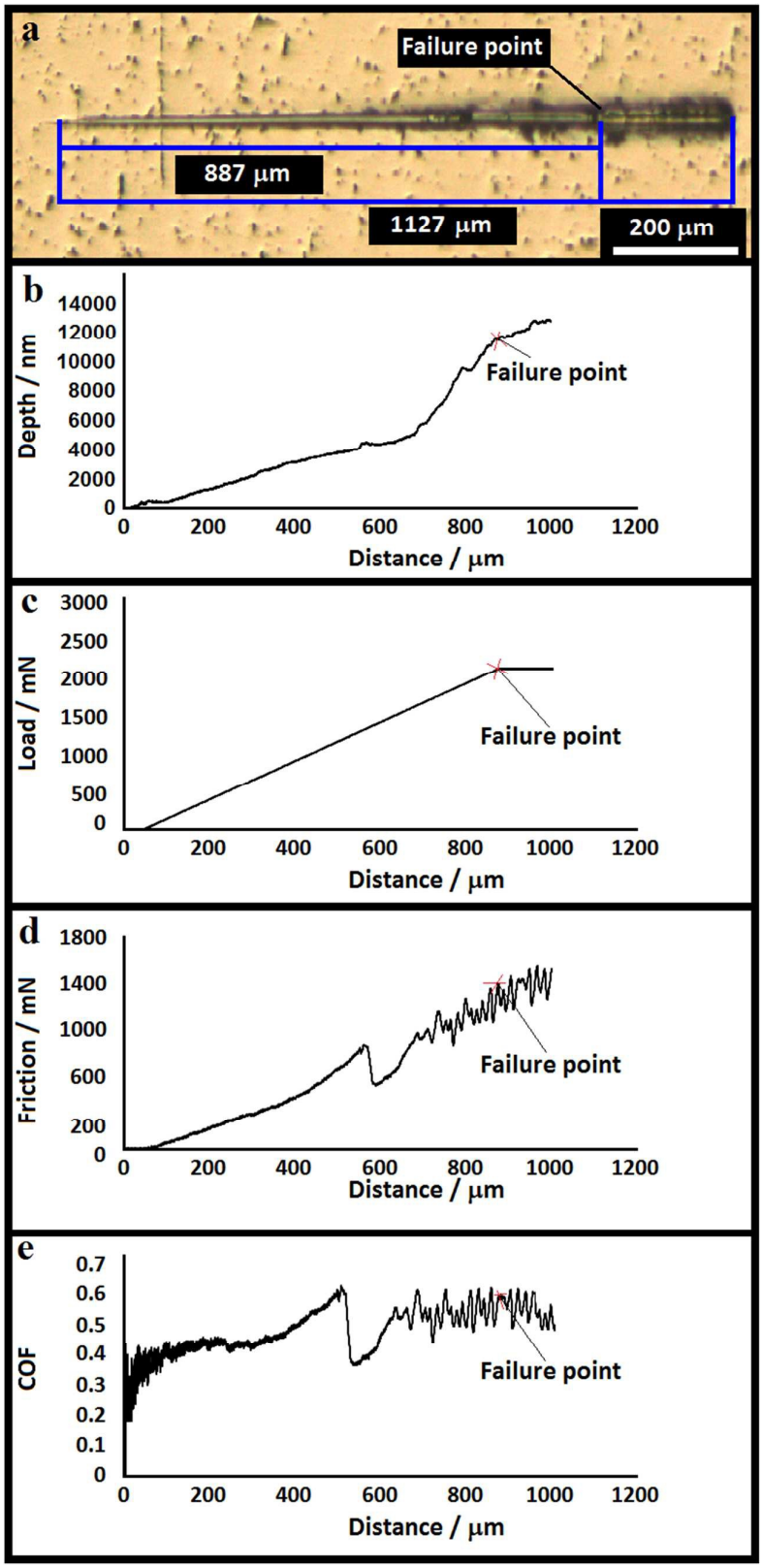

Fig. 11

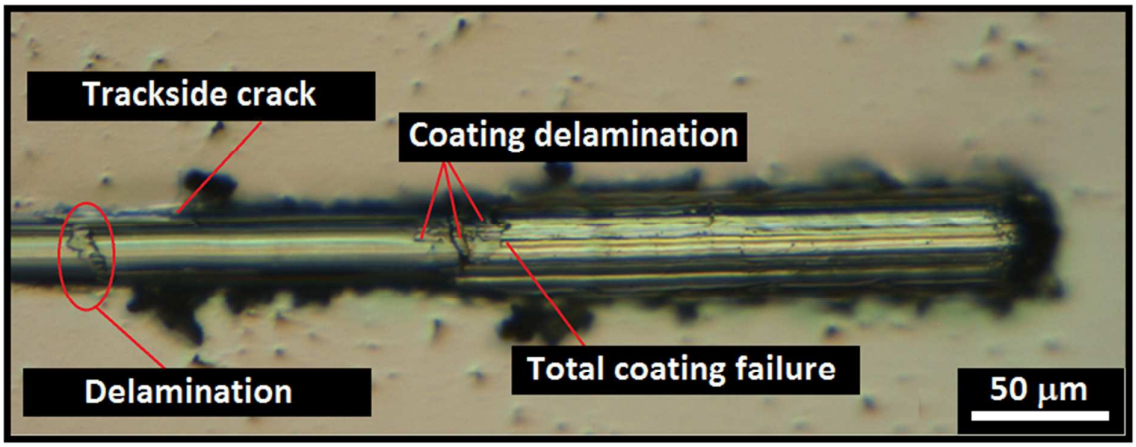

Fig. 12

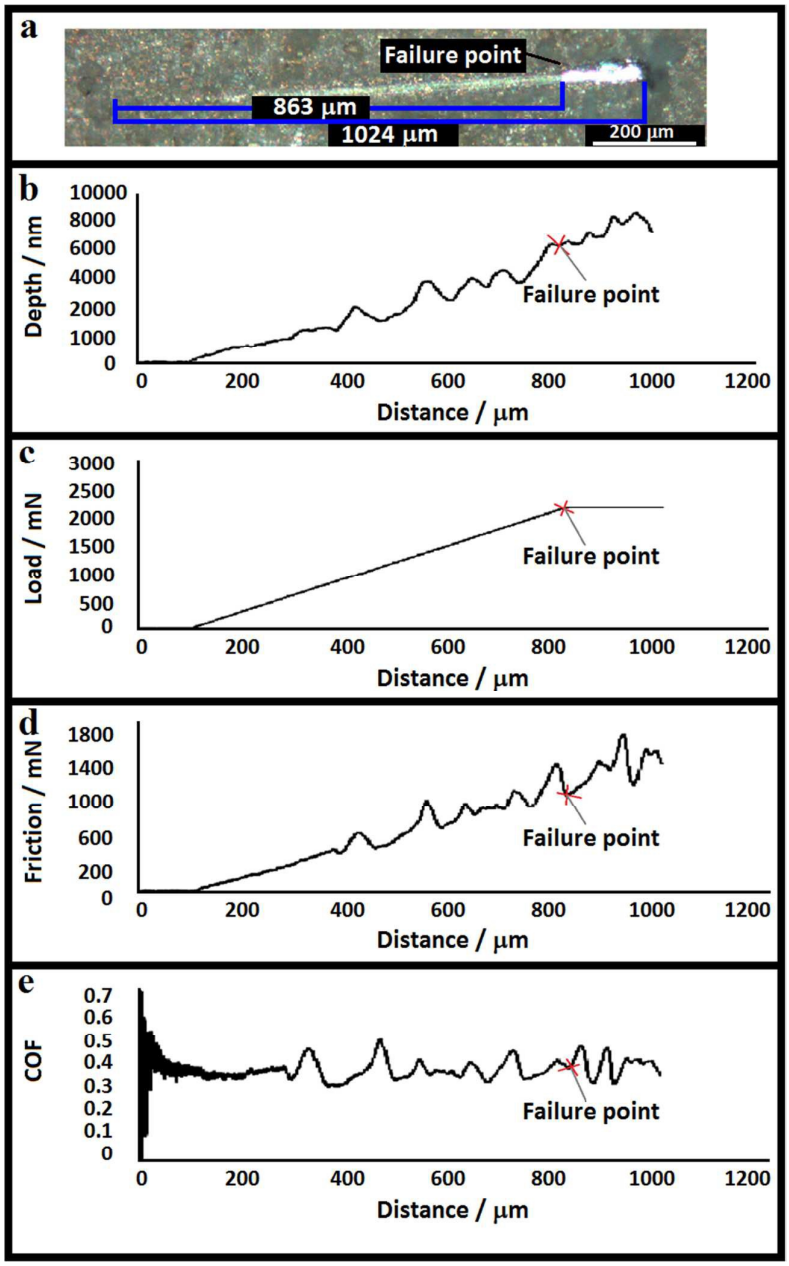

Fig. 13

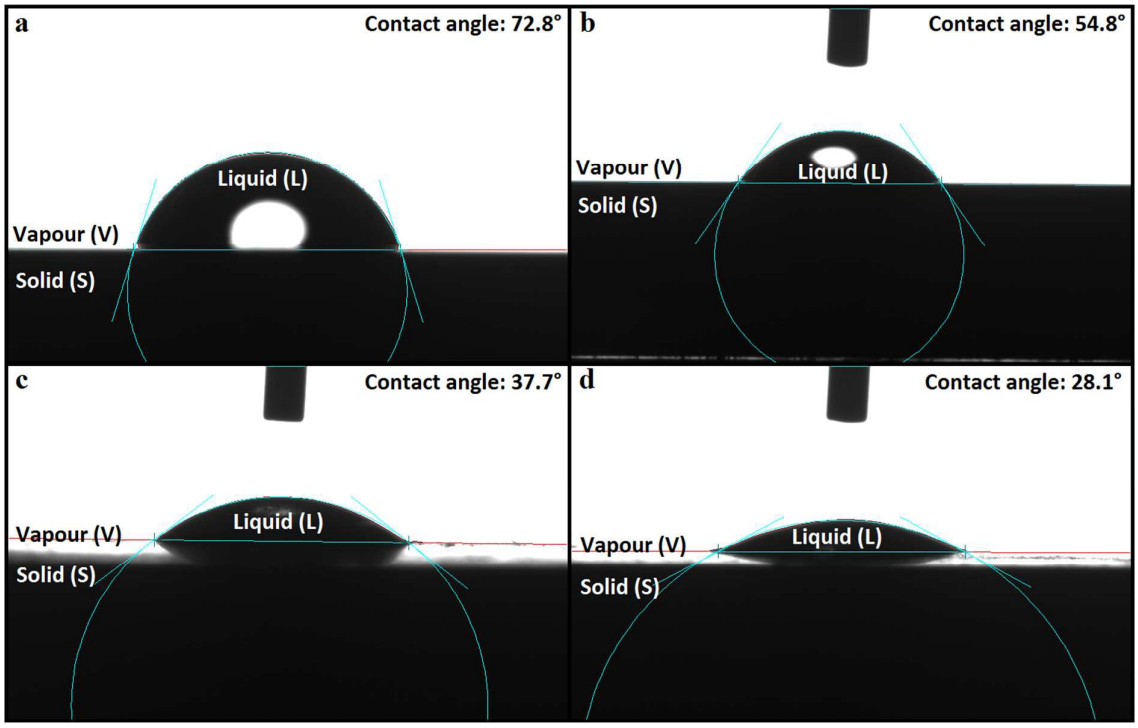

Fig. 14

Table 1 Different protocols used for synthesis of Ta_2O_5NTs via anodization technique.

No.	Electrolyte	Voltage (V)	Time (s)	Temp (°C)/ Time (h)	Size (μm)	Ref.
1	H_2SO_4 + 1.7%(v/v) HF (room temperature (one-step))	15	600	900 with NH_3 / 8	5	[19]
2	H_2SO_4 + 1%(v/v) HF (0° C (two-step))	15	600	900 with NH_3 / 8	2	[19]
3	H_2SO_4 + 1%(v/v) HF (0° C (optimized two-step))	25	300	900 with NH_3 / 8	270.3	[19]
4	1M H_2SO_4 + 2%wt HF (room temperature)	20	60	-	0.035	[20]
5	16 M H_2SO_4 + 0.2-0.9M HF (room temperature)	15	300	450 with H_2/ 5	1.2	[21]
6	HF/H_2SO_4 (1/9) + 0.1M H_3PO_4 (room temperature)	15	600	400 with O_2/ 3	1.3	[11]
7	HF/H_2SO_4 (1:9) + 5%(v/v) $C_2H_6O_2$ (room temperature))	10-15	1200	400 with O_2/ 3	5.1	[11]
8	HF/H_2SO_4 (1:9) + 5%wt C_2H_6OS (room temperature)	10-15	1200	300 with O_2/ 1	2.3-11.1	[11]
9	H_2SO_4 + 1% (v/v) HF + 4%(v/v) H_2O (0-50 °C)	50	1200	750 / 0.5	2.5	[22]
10	5.5ml HF + 223ml H_2SO_4 + 21.5ml H_2O (room temperature)	15	90	500 / 2	0.02-0.92	[16]
11	H_2SO_4 + 13.6%wt H_2O + 0.8%wt NH_4F (room temperature)	1.2*	2	1000 with NH_3 / 2	7.7	[23]
12	$C_2H_6O_2$ + 3%wt H_2O + 0.5%wt NH_4F (room temperature)	100	120	700 with NH_3 / 6	0.525	[24]
13	H_2SO_4 + 0.28%(v/v) HF + 4.29%(v/v) H_2O (room temperature)	30	300	750 with Ar /12	1.8	[25]
14	H_2SO_4 + 1.13%(v/v) HF + 5.17%(v/v) H_2O (room temperature)	30	300	750 with Ar / 12	4.8	[25]
15	H_2SO_4+ 0.2%(v/v) HF + 12%(v/v) H_2O (room temperature)	30	1200	750 with Ar / 12	35	[25]
17	2.9M HF + 16.4MH_2SO_4 (room temperature)	15	5-120	-	0.25-2.5	[26, 27]
16	HF/ H_2SO_4 (1:9) (room temperature)	10-40	600-1200	-	-	[28]
18	1M H_2SO_4 + 2%wt HF (room temperature)	20	14400	-	0.35-0.4	[29]

* Value is in terms of Acm^{-2}.

Table 2 The control parameters and their corresponding levels used in the experiments.

Experiment No.	DC power (W)	Temperature (°C)	Time (h)
1	250	200	2
2	250	250	4
3	250	300	6
4	300	200	4
5	300	250	6
6	300	300	2
7	350	200	6
8	350	250	2
9	350	300	4

Table 3 The measured scratch force and calculated *S / N* ratio.

Experiment No.	Scratch Force (mN)				*S / N* ratio
	1st	2nd	3rd	Mean	
1	812	823	833	823	58.31
2	1535	1479	1441	1485	63.42
3	1643	1702	1732	1692	64.56
4	1650	1632	1699	1660	64.40
5	1695	1714	1766	1725	64.73
6	1122	1236	1002	1120	60.89
7	1790	1821	1782	1798	65.09
8	1342	1450	1501	1431	63.08
9	1644	1656	1776	1692	64.55

Table 4 The *S / N* response values obtained for adhesion strength.

Coating Parameters	*S / N* ratio		
	Level1	Level2	Level3
DC power (W)	62.10	63.34	64.24
Temperature (°C)	62.26	63.74	63.33
Time (h)	60.76	64.12	64.79

Graphical Abstract

The proposed approach could be considered for the design of various nanostructured titanium implant surfaces.